Advanced nanoscale characterizations of solid oxide cell electrodes

Giuseppe Sassone, Ozden Celikbilek, Maxime Hubert, Katherine Develos Bagarinao, Thomas David, Laure Guetaz, Isabelle Martin, Julie Villanova, Lea Rorato, Bertrand Morel, et al.

Advanced Nanoscale Characterizations of Solid Oxide Cell Electrodes

G. Sassone[a], O. Celikbilek[a], M. Hubert[a], K. Develos-Bagarinao[b], T. David[c], L. Guetaz[c], I. Martin[d], J. Villanova[e], L. Rorato[a], B. Morel[a], A. Léon[f], J. Laurencin[a]

[a] Univ. Grenoble Alpes, CEA-Liten, DTCH, 38000 Grenoble, France
[b] Global Zero Emission Research Center, AIST, Tsukuba, Japan
[c] Univ. Grenoble Alpes, CEA-Liten, DTNM, 38000 Grenoble, France
[d] CAMECA Instruments Inc., 5470 Nobel Drive, Madison, Wisconsin 53711, United States
[e] ESRF the European Synchrotron, CS 40220, 38043, Grenoble Cedex 9, France
[f] European Institute for Energy Research (EIFER), Emmy-Noether Strasse 11, 76131 Karlsruhe, Germany

Solid oxide cells (SOCs) have attracted a growing attention thanks to their high efficiency and ability to operate in both electrolysis (SOEC) and fuel cell (SOFC) modes. Despite its great potential, the current SOC technology faces significant cell degradation during long-term operation. The degradation phenomena are still not well understood as they involve complex and intricate processes arising at different length scales. Additionally, it has been shown that the degradation rate under SOEC operation is generally higher than in SOFC mode. To address this issue, durability tests were performed in SOEC mode at 750, 800 and 850 °C for 2000 h at -1 A cm^{-2} in 10/90 vol.% H_2/H_2O and dry air. The electrochemical performance of the cells was assessed using electrochemical impedance spectroscopy. In addition, advanced characterization techniques with nanometer and atomic resolution have been used to study material degradation after long-term testing.

Introduction

The growing interest in the transition towards a fossil-free energy system has accelerated research and development on hydrogen-based energy conversion technologies. In this context, solid oxide cells (SOCs) have attracted attention as they can be operated in both fuel cell (SOFC) and electrolysis (SOEC) modes providing a clean and sustainable way of producing both green hydrogen and electricity at high efficiency. Despite their great potential, the current SOC technology faces some challenges due to significant cell degradation upon operation. The SOC degradation is strongly dependent on the operating temperature (1), the current density (2–4) and the humidity content in the air (5–8). Besides, the degradation in SOEC mode is substantially higher than in SOFC operation for electrode supported cells (9, 10). The performance loss has been attributed to several factors, such as microstructural evolution in the electrodes (11–13), active site poisoning (14–16), inter-diffusion of elements between the cell layers and formation of secondary phases (e.g. $SrZrO_3$) associated to material decomposition and reactivity at the interfaces (9, 17–20).

In this work, the durability of a hydrogen electrode supported cell made of the standard materials has been investigated under electrolysis operation. Following the long-term operations, post-test characterizations were performed at various length scales to understand the degradation phenomena in the different cell layers and assess their impact on the performance. Herein, the effect of temperature on the cell degradation has been studied. To this end, three cells were aged at 750, 800 and 850 °C for 2000 h in SOEC mode at -1 $A \cdot cm^{-2}$ using dry air as sweep gas at the oxygen electrode side. The electrochemical behavior of the cells has been characterized using electrochemical impedance spectroscopy (EIS) and polarization curves acquired at a reference temperature (750 °C). The advanced post-test characterizations include techniques such as 3D focused ion beam-scanning electron microscope (3D FIB-SEM), high-resolution secondary ion mass spectroscopy (SIMS) imaging, synchrotron-radiation-based X-ray diffraction (nano-XRD) and X-ray fluorescence (nano-XRF), scanning transmission electron microscopy (STEM) coupled with energy-dispersive X-ray spectroscopy (EDS), and atom probe tomography (APT).

Materials and methods

Cell description. The tested hydrogen electrode supported cells are composed of a $La_{0.6}Sr_{0.4}Co_{0.2}Fe_{0.8}O_{3-\delta}$ (LSCF) current collecting layer (CCL) and an LSCF-$Ce_{0.8}Gd_{0.2}O_{2-\delta}$ (LSCF-GDC) composite functional layer (FL) for the oxygen electrode, GDC for the barrier layer (BL), $Y_{0.16}Zr_{0.84}O_{1.92}$ (8YSZ) for the electrolyte and Ni-YSZ for the hydrogen electrode. The cells have a circular shape and an active area of 9.08 cm^2. The CCL and FL are both ≈ 20 µm, the BL is ≈ 3 µm, the electrolyte is 8 µm. The cermet is composed of a thick Ni-3YSZ substrate (≈ 280 µm) and a thin Ni-8YSZ functional layer (≈ 25 µm). In the following, the as-received cell is referred to as the reference and the cells that have been operated at high-temperatures and under current for a long period of time are referred to as aged samples and their corresponding temperature.

Long-term tests and electrochemical characterizations

Experimental setup. An in-house test bench was used for the long-term operation of the cell. The circular cell was placed in a metallic housing inside a furnace. The gas tightness of the fuel compartment was ensured by a glass ceramic sealant (Schott G018-311) deposited at the cell periphery (20, 21). Afterwards, the furnace was heated up to 860 °C with a heating rate of 1 $°C \cdot min^{-1}$ and maintained at this temperature for 90 min to complete the glass sealing formation. During this step, 0.5 $Nl \cdot h^{-1}$ of N_2 and 0.5 $Nl \cdot h^{-1}$ of dry compressed air, compliant with class [1:1:1] according to ISO 8573-1, were supplied at the hydrogen and oxygen electrodes, respectively. Subsequently, the flows at the two electrodes were then increased to 4 $Nl \cdot h^{-1}$ and the temperature was decreased to 800 °C to perform the reduction of Ni-YSZ cermet. The N_2 was progressively substituted with H_2 during the reduction protocol. When the N_2 was completely substituted with H_2, the cell was maintained under these conditions for a minimum of 16 h. Thereafter, initial electrochemical characterizations were carried out before starting the long-term tests. At the end of the tests, the cells were cooled down to room temperature at a rate of 1 $°C \cdot min^{-1}$. During the cooling, a mixture of nitrogen and hydrogen was supplied to the hydrogen electrode to maintain the cermet in its reduced state and to avoid possible re-oxidation.

Long-term tests. In this study, the long-term tests were performed for 2000 h in galvanostatic mode at a fixed current density of -1 $A \cdot cm^{-2}$ in SOEC mode, 64% steam conversion (SC). In order to assess the effect of temperature on the cell durability, three long-term tests were performed at 750, 800 and 850 °C. During these experiments, 36 $NmL \cdot min^{-1} \cdot cm^{-2}$ of dry compressed air was supplied to the oxygen electrode side. The inlet flow at the hydrogen electrode was set to 12 $NmL \cdot min^{-1} \cdot cm^{-2}$ with a composition of 10/90 H_2/H_2O.

Electrochemical measurements. Before and after the long-term tests, electrochemical impedance spectroscopy (EIS) was performed at a reference condition (i.e. 750 °C and 10/90 H_2/H_2O at the fuel side). This protocol was set in order to assess the degradation in a reference condition for comparing the ageing tests carried out at different temperatures (750, 800, 850°C). The EIS were acquired using a potentiostat/galvanostat (Autolab PGSTAT-302N) equipped with a frequency response analyzer module (FRA) and a 20 A current booster. The EIS measurements were performed at open circuit voltage (OCV) by imposing a sinusoidal current with an amplitude of 100 mA in the frequency range of 10^{-2} to 10^4 Hz. The raw impedance spectra were collected using the NOVA ver. 1.11 software.

Post-test characterizations

3D FIB-SEM. 3D FIB-SEM data were acquired on a Zeiss Crossbeam 550. For each sample, a volume of a few tenths of microns was imaged in the three dimensions with a pixel size of 10 nm and an inter-slice distance of 10 nm, resulting in a cubic voxel of 10x10x10 nm^3. The FIB milling was performed at 30 kV with a current of 3 nA, and the electron column was operated at 1.5 kV and 1 nA. Images from InLens and SE2 detectors were acquired simultaneously. Image processing prior to segmentation included slice-to-slice alignment, contrast/brightness homogenization in all three directions, curtain effect correction and resampling in the z-direction to correct for non-homogeneous inter-slice distances during milling and imaging. These steps were done using home-made Python scripts based on common image processing Python libraries (e.g. numpy, scikit-image, etc.). The segmentation was performed using machine learning based a on random forest classifier with Ilastik software (20, 22) using the 'pixel classification' workflow. The annotation and training phase were done on sub-volumes of 100-300 pixels in each direction.

SIMS imaging. The elemental composition distribution of the reference and aged samples was investigated using high-resolution secondary ion mass spectrometry imaging analysis apparatus (SIMS, NanoSIMS 50L, Ametek CAMECA). The samples were infiltrated with a high-vacuum-compatible resin, and the cross-section surfaces were subsequently polished using diamond slurry. During the measurements, a Cs^+ primary ion beam with a beam diameter of ≈ 100 nm and beam current of ≈ 23 nA was used to scan the cross section. For both electrodes, the analyzed region of interests (ROIs) include the functional layer and a part of the electrolyte (raster areas: 20 μm × 20 μm and 10 μm × 10 μm). Representative secondary ion mass species for the cell elements were detected simultaneously via a multicollection system. The image processing was done using WinImage ver. 4.6 software (Ametek, Cameca).

Synchrotron characterizations. The lamellae for the synchrotron nano-XRD and nano-XRF were prepared using a Xe^+ plasma-Focused Ion Beam (pFIB) Vion (FEI™), following a similar protocol as detailed in references (20, 23). Pieces of reference and aged cells were positioned in the vacuum chamber of the PFIB machine to prepare the lamellae with dimensions equal to approximately 60 × 60 × 2 μm^3 for the horizontal dimension (X), the vertical dimension (Y) and the depth (Z), respectively. A 10 µm Pt protective layer was deposited on top of the electrode, then the lamellae were fixed on an aluminum pin. The XRF and XRD analyses were performed at the ID16B beamline in the European Synchrotron Radiation Facility (ESRF) (24). The beamline provides a high flux (10^{12} ph/s) focused X-ray beam, with a spot size of 60×60 nm^2. An energy of 29.6 keV was selected for this study in order to analyze all the cell elements. A ROI of 7×8 μm^2 was defined at the LSCF-GDC/GDC/YSZ interfaces to focus on the elemental inter-diffusion. Both XRF and XRD 2D maps were acquired with a step of 50 nm and an exposure time of 1000 ms per point. PyMca software (25) was used to fit the XRF data and the diffraction data were treated with XRDUA software (26). The line profile for each XRF elemental maps were extracted by averaging the line on the horizontal scale.

STEM-EDS. STEM/EDS analyses were performed using a FEI-Themis microscope equipped with a probe aberration corrector and a super-X detection system. The samples were prepared by embedding in an epoxy resin. Thin lamellae were then extracted by FIB in the LSCF-GDC/GDC/YSZ area. Using the Esprit Bruker Software, semi-quantitative analyses were done on the line profiles using the Cliff-Lorimer method applied on the Y and K lines, and Ce, Zr and Gd L lines. The analyses were carried out on the reference sample and the sample aged at 800 °C.

APT. Atom probe tomography was performed on a CAMECA LEAP 6000XR atom probe. Atom probe specimens were prepared from the interface of the LSCF-GDC/GDC/YSZ on a Helios 660 FIB-SEM using standard top down liftout methodology **(27)**. Data was acquired using a pulsed laser operated at 30 pJ and 100 kHz, a detection rate of 1%, and temperature of 30K. Data was analyzed by CAMECA's AP Suite 6.3 Analysis software. The analyses were carried out on the reference sample and the sample aged at 800 °C.

Results and discussion

Durability test and electrochemical characterizations

The electrochemical characterizations were carried out at 750, 800 and 850 °C in SOEC mode at -1 $A \cdot cm^{-2}$, 64 % SC, 10/90 vol.% H_2/H_2O composition. The evolution of the impedance spectra is shown in Figure 1. The measurements at OCV were conducted before and after the end of the experiment at 750 °C as a reference temperature. The Nyquist plots indicate three arcs in high-frequency (HF, >1 kHz), mid-frequency (MF, 1 Hz - 1 kHz) and low-frequency (LF, <1 Hz) regions. A physic-based multi-scale model was used to identify each contribution. The arcs at HF, MF and LF were mainly attributed to the hydrogen electrode, oxygen electrode, and gas conversion, respectively (28). The evolution of the EIS diagrams after ageing is more pronounced in the high frequency region for all cells, whereas the mid- and low-frequency regions remain almost unchanged. This suggests that the majority of the deterioration is likely to be associated

to the hydrogen electrode. It is worth noting that the evolution of the polarization resistance in the high-frequency region was accompanied by a significant increase in the ohmic resistance. The increase of both resistances is commonly ascribed to both Ni agglomeration and Ni migration away from the electrolyte interface (29, 30). On the contrary, the fact that the MF contribution does not change with time suggests that the oxygen electrode degradation remains limited at all operating temperatures.

The evolution of the cell voltage over time, as seen in Figure 1a, indicates that the rate of degradation for all cells is higher during the first 800 hours. After this initial period, the degradation rate slows down to reach an asymptotic value around 2.8, 1.1 and 0.6 %/kh for the cells aged at 750, 800 and 850 °C, respectively. Therefore, the 'apparent' degradation rate measured on the durability curve decreases as the temperature increases. However, the EIS spectra measured at the same temperature before and after the test reveal that the highest 'intrinsic' degradation in terms of both series and polarization resistances is obtained at the highest operating temperature (850 °C). As discussed in (20, 31), this result implies that the material degradation is enhanced by the temperature, which is an aggravating factor. It can be noticed that the lower 'apparent' degradation rate measured at higher temperature can be explained by the electrode activation overpotentials, which are strongly thermally activated. In this condition, the contribution of the activation losses in the whole cell resistance becomes less and less pronounced with increasing the temperature, in such a way that the impact of electrode degradation is less visible in the durability curve (recorded during ageing at the operating temperature). Therefore, it is essential to assess the degradation in a reference condition before and after the test.

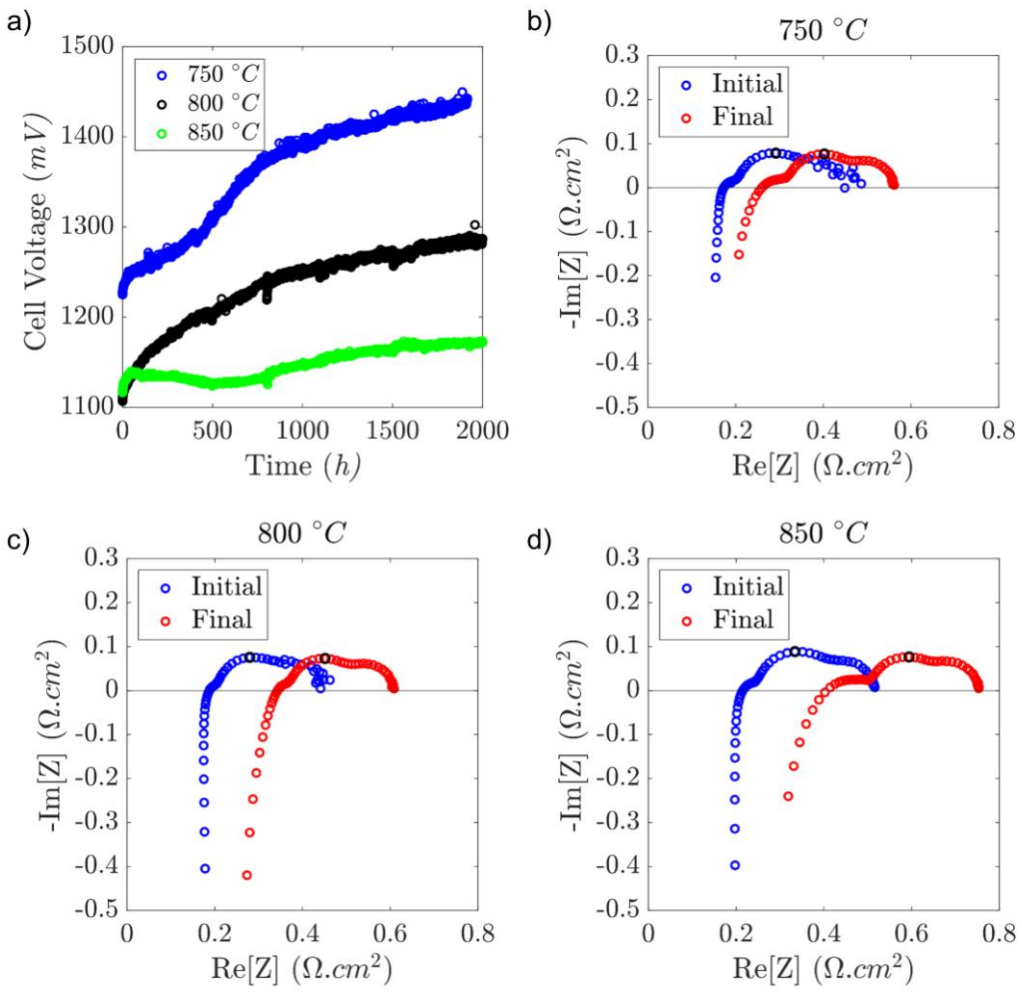

Figure 1. a) Experimental durability curves showing the cell voltage degradation for the cells aged at the three operating temperatures (750°C, 800°C and 850°C) for 2000 h in SOEC mode at -1 A·cm^{-2}, 64% SC, 10/90 vol.% H_2/H_2O. Impedance spectra measured at b) 750 °C, c) 800 °C and d) 850°C before and after 2000 h ageing. The maximum frequency of the impedance spectra remains constant around ≈ 2 Hz and are indicated by the black circles in the figures.

Post-mortem characterizations

Figure 2 shows typical images acquired using high-resolution SIMS analyses, depicting the Ni distribution in the vicinity of the YSZ/Ni-YSZ interfaces of the reference and aged samples. It can be noticed that Ni particles migrate away from the interface towards the bulk of the Ni-YSZ electrode with ageing. Ni particles gradually agglomerate into larger particles with increasing temperature. Moreover, the Ni depletion is clearly enhanced with increasing temperature. This observation suggests that increasing the temperature from 750°C to 850°C facilitates Ni migration. This behavior could be explained by a higher Ni surface diffusion coefficient (32). In agreement with the electrochemical characterizations, the post-test characterizations showed that most of the

degradation in SOEC mode was related to a strong Ni depletion in the hydrogen electrode near the YSZ interface. Therefore, the Ni depletion explains the increase of both the ohmic resistance and high-frequency arc resistance in the impedance spectra.

Microstructural characterizations were performed by 3D FIB-SEM reconstructions (not shown here). The 3D volumes have also confirmed the strong Ni migration which is enhanced by the temperature. This microstructural evolution induces a loss of the active triple phase boundary length (TPBl) density. Indeed, the TPBl was calculated as 2.85, 2.57, 1.72 and 1.31 μm^{-2} for the reference and the samples aged at 750, 800 and 850 °C, respectively. Besides, Ni particle size has also been found to increase with increasing operating temperature. The Ni particle diameter was calculated to be 0.57, 0.67, 0.76 and 0.79 µm for the reference and the samples aged at 750, 800 and 850 °C, respectively.

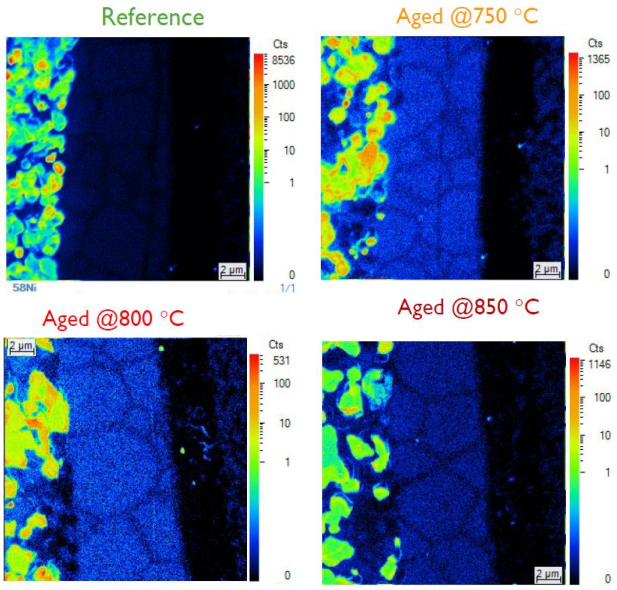

Figure 2. Ni agglomeration and Ni migration detected in the hydrogen electrode by SIMS performed on the reference sample and the samples aged at 750, 800 and 850 °C.

The oxygen electrode and the barrier layer were also thoroughly analyzed using nanoscale synchrotron techniques. 1D elemental line profiles extracted from the nano-XRF maps are displayed in Figure 3. The scanned zones include LSCF-GDC/GDC/YSZ interfaces. A few key points emerge from the figures. Firstly, for all samples, the La, Sr, Co and Fe signals from the oxygen electrode begin to decrease in the BL, but then tend to increase near the YSZ layer. This trend is particularly pronounced for Sr and Co. While the Sr profile shows a smooth increase only around the GDC/YSZ interface, some spikes in the intensity profile are observed for Co at the BL and GDC/YSZ interface, suggesting individual Co oxide particles. Secondly, a Gd-rich layer can be identified near the GDC/YSZ interface for all samples. Lastly, Y and Zr signals from the YSZ layer also demonstrate diffusion in the opposite direction towards the BL. This zone (around the zero in Figure 3) can be identified as the inter-diffusion layer (IDL). There was no apparent evolution detected in the IDL following a 2000-hour aging period at the three operating temperatures. As observed in the reference sample, elemental migration already

occurs during the cell manufacturing. All these observations are in agreement with previous works (18, 33). For instance, similar to our work, Villanova et al. (18) studied the elemental migrations in hydrogen electrode supported cells consisting of LSCF/GDC/YSZ/Ni-YSZ, before and after 6100 h of test in electrolysis mode. They found that Sr diffused through the BL and formed a dense layer of ≈ 0.7 µm at the GDC/YSZ interface, whereas La was found to be homogeneously distributed throughout the BL. Similar to our results, Co was found to exist in the BL in the form of individual particles. The authors did not find an evident evolution before and after aging tests. It is important to note that the signal intensity is highly dependent on the lamella thickness. Therefore, the results can only be qualitatively compared. It is worth noting that all these results are also consistent with the electrochemical characterizations, which have shown that the oxygen electrode response is not significantly impacted by the long-term operation.

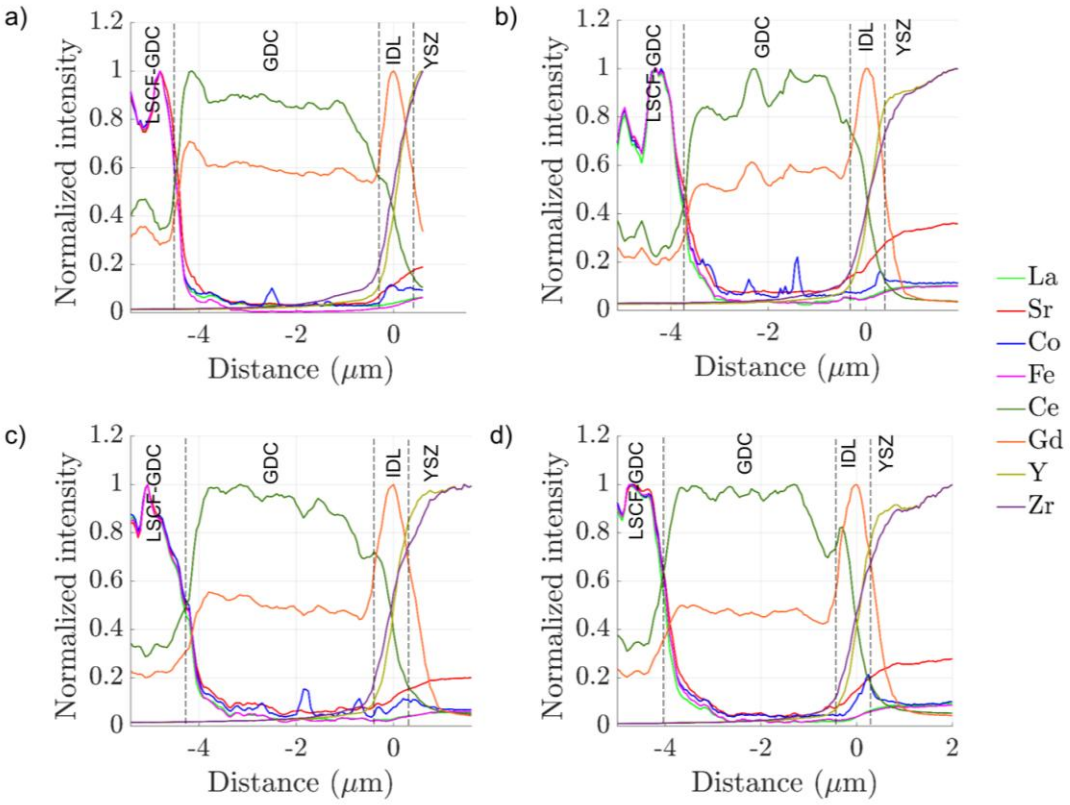

Figure 3. Elemental line profiles measured by nano-XRF across the LSCF-GDC/GDC/YSZ interfaces for the a) reference sample and the samples aged in SOEC mode at b) 750 °C, c) 800 °C and d) 850 °C. The scans were done on a 7x8 µm^2 area with 50 nm spot size. The highest Gd intensity was chosen as the zero coordinate.

The crystallographic information from the same area was obtained by nano-XRD measurements. The XRD patterns are shown in Figure 4. In general, the diffractograms contain only LSCF, GDC and YSZ phases. The LSCF phase was accurately matched

with a rhombohedral phase having the $R\bar{3}c$ space group (no. 167). GDC and YSZ were well-matched with a cubic phase having the $Fm\bar{3}m$ space group (no. 225). In between GDC and YSZ phases, intermediate peaks were observed that were attributed to the IDL (34, 35). It is important to note that $SrZrO_3$ phase formation was not identified. In addition, it should be noted that the SrO identification is hindered due to the fact that its lattice parameter value (i.e. 5.16 Å) lies in between those of YSZ (5.14 Å) and GDC (5.42 Å). Moreover, this zone also contains the phases related to the IDL (36).

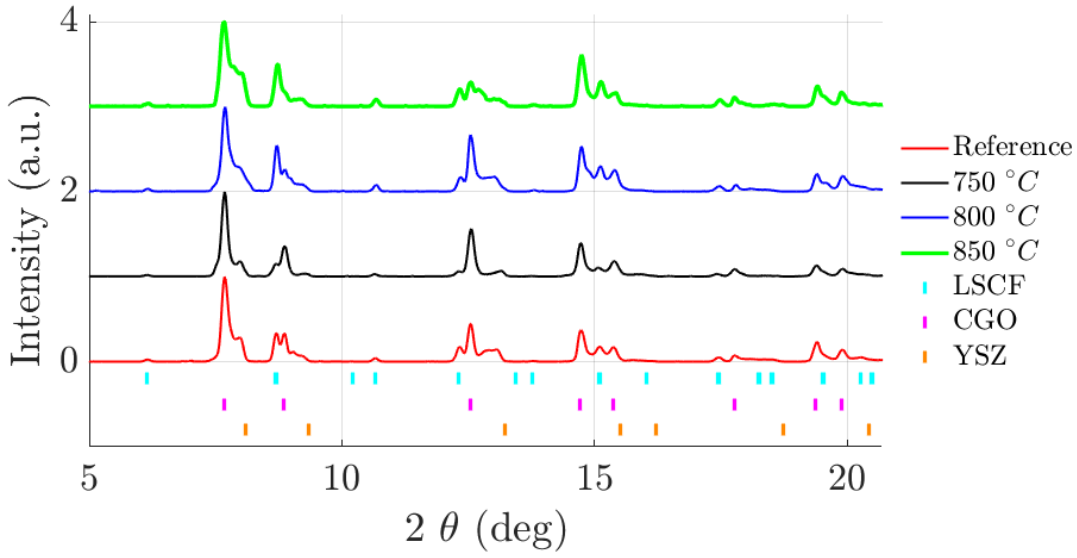

Figure 4. X-ray diffractograms of a) reference cell, b) aged cell at 750 °C for 2000 h under electrolysis mode, near the GDC/YSZ interface focusing on the IDL. The color-coded phase identification is indicated with vertical lines.

To obtain further information on the elemental inter-diffusion and the composition of the IDL, STEM-EDS elemental mapping was performed near the GDC/YSZ interface of the reference sample and the sample aged at 800 °C (Figure 5). Ce, Gd, Zr and Y maps are shown. It is important to note that Sr signal was not detected. The HAADF images show that the IDL consists of a dense zone indicated by dashed lines. The reference sample in Figure 5a shows one layer of 600 nm-thick grains, whereas the aged sample in Figure 5b shows two layers of 1 µm-thick grains. It is not yet clear whether this is a general trend along the entire cell, as the lamellae for the measurements represent a small, localized zone. Therefore, further studies are needed to confirm these results. Line profiles were extracted from the EDS elemental maps, and then a semi-quantitative analyses were performed using the Cliff-Lorimer method in order to show the evolution of the Zr, Y, Ce and Gd (in at.%). Both cells show a gradual decrease in Ce, whereas Gd is maintained constant in the IDL. It can also be seen that Zr and Y diffuse from YSZ into the IDL. In agreement with nano-XRF measurements, the IDL seems to have formed in the reference sample during the cell manufacturing. Similarly, $SrZrO_3$ phase was not detected in these observations.

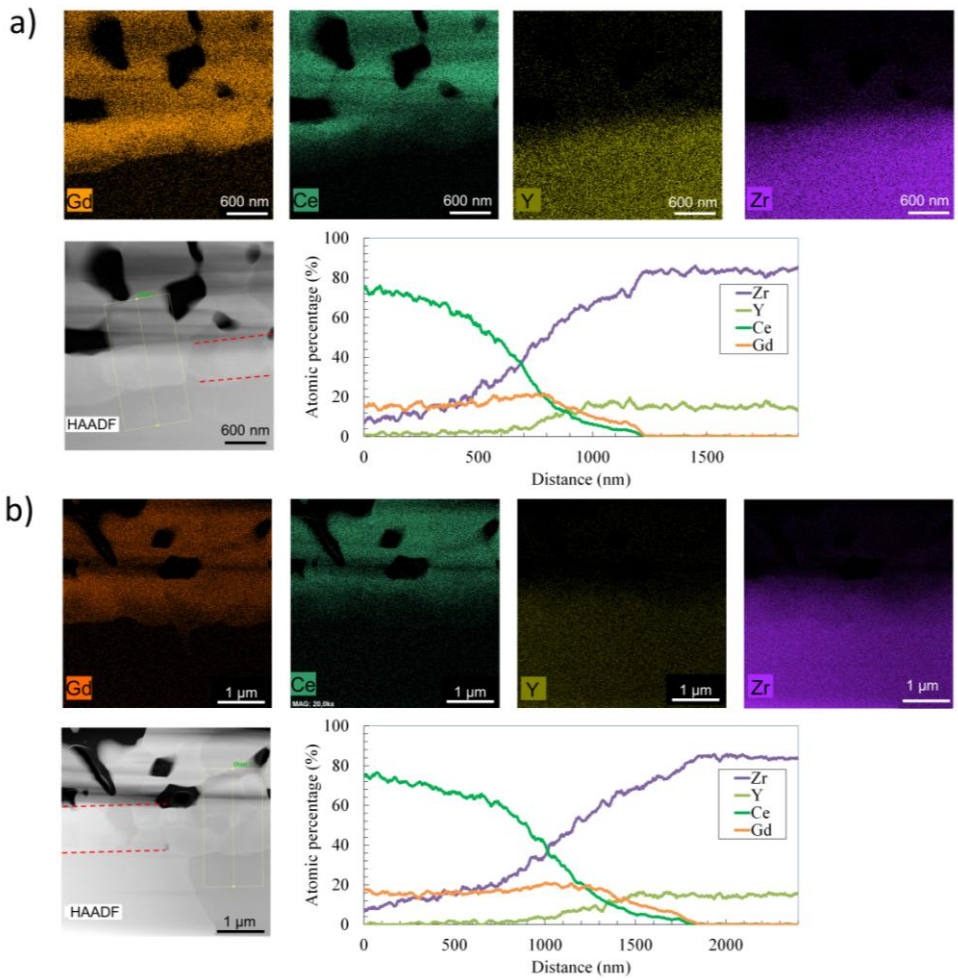

Figure 5. STEM-EDS elemental maps (Ce, Gd, Zr) focused on the GDC/YSZ interface: a) reference sample, b) the sample aged at 800 °C. The STEM-EDS line profiles (in at.%) below show the evolution of the different elements across the GDC/YSZ interface.

In complementarity with the STEM-EDS characterization, the APT technique was used to visualize how the diffusing elements are distributed in the barrier layer in 3D at the atomic scale resolution. Figure 6 displays two GDC grains and the grain boundary between them. For both cells, Fe, Co and Sr diffuse mainly through the grain boundaries. On the other hand, La diffusion occurs both in the bulk of the grains and along the GDC grain boundaries. It is important to note that the positions at which the specimens were extracted from both cells do not represent the same zone. For instance, two GDC grains in the reference sample were extracted from the BL closer to the YSZ interface, whereas they were closer to the oxygen electrode in the aged sample. Therefore, a quantitative comparison is avoided in this study.

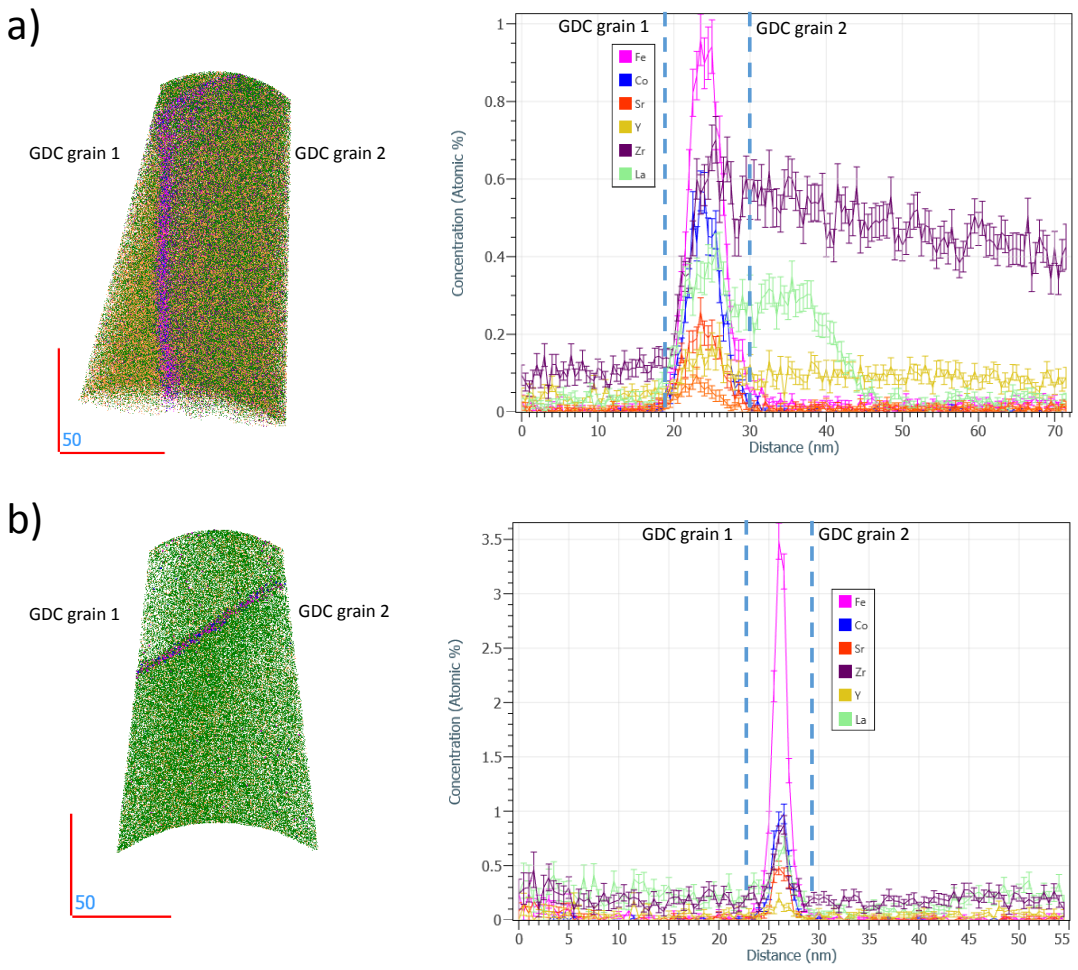

Figure 6. Atomic-map of two GDC grains and 1D line profile orthogonal to the grain boundary obtained from APT analyses on a) the reference sample and b) the sample aged at 800 °C for 2000 h.

Overall, all of the advanced characterization techniques presented in this work have demonstrated inter-diffusion of elements from the oxygen electrode side to the electrolyte and from the electrolyte to the barrier layer. Nevertheless, an extensive formation of an insulating phase such as $SrZrO_3$ was not detected. Previous works suggest that manufacturing conditions, in particular the sintering temperature, play a role in the formation and thickness of the IDL, which in turn affects the $SrZrO_3$ formation (17, 37, 38). The most distinct phase formations were found near the GDC/YSZ interface, which was referred to as inter-diffusion layer (IDL). Although the function of the IDL is not yet fully understood, it has been speculated to inhibit or mitigate the $SrZrO_3$ formation during operation (17). The elemental inter-diffusion after manufacturing does not significantly increase after long-term operation. This statement is in good agreement with the good stability of the oxygen electrode polarization resistance upon operation. Considering all these results, it appears that the cell performance degradation is mostly due to the microstructural changes in the hydrogen electrode.

Conclusions

In this work, the influence of operating temperature on the cell durability was investigated in SOEC mode. The study includes electrochemical tests at 750, 800, 850 °C for 2000 h in SOEC mode at -1 A cm^{-2}, 10/90 vol.% H_2/H_2O and using dry air as sweep gas at the oxygen electrode side. The degradation was assessed by impedance spectra recorded in the same conditions before and after the test for all experiments. The analyses have revealed that the 'intrinsic' degradation is enhanced with increasing operating temperatures. Besides, the evolution of both the ohmic losses and the HF arc related to the hydrogen electrode are the main consequences of the ageing on the EIS. Conversely, the MF contribution attributed to the oxygen electrode is not affected by the long-term operation. Advanced post-test characterizations following the durability tests revealed a strong evolution of the hydrogen electrode microstructure, which was the primary cause of the degradation. It has been highlighted that the Ni migration away from the electrolyte was accelerated from 750°C to 850°C. Regarding the oxygen electrode, synchrotron-based nano-XRF measurements revealed the diffusion of Sr and Co elements towards the YSZ electrolyte in the pristine cell. This Sr and Co migration does not seem to evolve significantly upon operation. Further investigations near the barrier layer and the electrolyte revealed an IDL containing mainly Gd, Ce and Zr for both the reference and the aged samples. The IDL formation in all the samples was also confirmed by synchrotron-based nano-XRD measurements.

STEM-EDS characterizations have also highlighted the elemental intermixing in the IDL. The chemical analyses have shown that the IDL was a solid solution composed mainly of Gd, Ce and Zr. Finally, APT technique was performed to obtain a 3D distribution of elements near the barrier layer. APT has unveiled that the oxygen electrode elements (La, Sr, Co and Fe) diffused through the grain boundaries of the GDC towards the YSZ electrolyte. All these advanced techniques confirmed that the elemental intermixing and the formation of IDL already occurred during the cell manufacturing. However, the formation of the insulating phases such as $SrZrO_3$ has not been detected in all the samples. These results are consistent with the good stability of the oxygen electrode response measured before and after the test. This behavior could be correlated to the IDL already present in the as-received (reference) cell, which could limit further inter-diffusion of elements during long-term operation.

Acknowledgments

This project has received funding from the Fuel Cells and hydrogen 2 Joint Undertaking (JU) under grand agreement n°874577 (NewSOC project). The work has also been supported by Genvia, the projects CELCER-EHT from the National Research Agency (grant agreement ANR-PEHY-008, France 2030) and CASSIOPEE from Carnot Energie du Futur. The nano-XRF and nano-XRD experiments (proposal ID MA5526) were carried out at the ID16B beamline in European Synchrotron Radiation Facility (ESRF), France.

References

1. C. Endler-Schuck, A. Leonide, A. Weber, S. Uhlenbruck, F. Tietz, and E. Ivers-Tiffée, *Journal of Power Sources*, **196**, 7257–7262 (2011).
2. R. Knibbe, M. L. Traulsen, A. Hauch, S. D. Ebbesen, and M. Mogensen, *J. Electrochem. Soc.*, **157**, B1209 (2010).
3. M. Z. Khan, R.-H. Song, A. Hussain, S.-B. Lee, T.-H. Lim, and J.-E. Hong, *Journal of the European Ceramic Society*, **40**, 1407–1417 (2020).
4. M. Z. Khan, M. T. Mehran, R.-H. Song, S.-B. Lee, and T.-H. Lim, *International Journal of Hydrogen Energy*, **43**, 12346–12357 (2018).
5. E. Bucher and W. Sitte, *Solid State Ionics*, **192**, 480–482 (2011).
6. P. Hjalmarsson, M. Søgaard, and M. Mogensen, *Solid State Ionics*, **179**, 1422–1426 (2008).
7. M. Kim, H. Muroyama, T. Matsui, and K. Eguchi, *J. Electrochem. Soc.*, **166**, F1269 (2019).
8. R. R. Liu, S. H. Kim, S. Taniguchi, T. Oshima, Y. Shiratori, K. Ito, and K. Sasaki, *Journal of Power Sources*, **196**, 7090–7096 (2011).
9. J. Laurencin, M. Hubert, D. F. Sanchez, S. Pylypko, M. Morales, A. Morata, B. Morel, D. Montinaro, F. Lefebvre-Joud, and E. Siebert, *Electrochimica Acta*, **241**, 459–476 (2017).
10. C. E. Frey, Q. Fang, D. Sebold, L. Blum, and N. H. Menzler, *J. Electrochem. Soc.*, **165**, F357 (2018).
11. F. Monaco, M. Hubert, J. Vulliet, J. P. Ouweltjes, D. Montinaro, P. Cloetens, P. Piccardo, F. Lefebvre-Joud, and J. Laurencin, *J. Electrochem. Soc.*, **166**, F1229 (2019).
12. E. Lay-Grindler, J. Laurencin, J. Villanova, P. Cloetens, P. Bleuet, A. Mansuy, J. Mougin, and G. Delette, *Journal of Power Sources*, **269**, 927–936 (2014).
13. D. Simwonis, F. Tietz, and D. Stöver, *Solid State Ionics*, **132**, 241–251 (2000).
14. A. Hauch, S. H. Jensen, J. B. Bilde-Sørensen, and M. Mogensen, *J. Electrochem. Soc.*, **154**, A619 (2007).
15. B. Wei, K. Chen, L. Zhao, Z. Lü, and S. P. Jiang, *Phys. Chem. Chem. Phys.*, **17**, 1601–1609 (2014).
16. J. A. Schuler, H. Yokokawa, C. F. Calderone, Q. Jeangros, Z. Wuillemin, A. Hessler-Wyser, and J. Van herle, *Journal of Power Sources*, **201**, 112–120 (2012).
17. F. Wankmüller, J. Szász, J. Joos, V. Wilde, H. Störmer, D. Gerthsen, and E. Ivers-Tiffée, *Journal of Power Sources*, **360**, 399–408 (2017).
18. J. Villanova, S. Schlabach, A. Brisse, and A. Léon, *Journal of Power Sources*, **421**, 100–108 (2019).
19. S. Uhlenbruck, T. Moskalewicz, N. Jordan, H.-J. Penkalla, and H. P. Buchkremer, *Solid State Ionics*, **180**, 418–423 (2009).
20. F. Monaco, D. Ferreira-Sanchez, M. Hubert, B. Morel, D. Montinaro, D. Grolimund, and J. Laurencin, *International Journal of Hydrogen Energy*, **46**, 31533–31549 (2021).
21. E. Da Rosa Silva, G. Sassone, M. Prioux, M. Hubert, B. Morel, and J. Laurencin, *Journal of Power Sources*, **556**, 232499 (2023).
22. C. Sommer, C. Straehle, U. Köthe, and F. A. Hamprecht, in *2011 IEEE International Symposium on Biomedical Imaging: From Nano to Macro*,, p. 230–233 (2011).

23. N. I. Khamidy, J. Laurencin, D. Ferreira Sanchez, F. Monaco, F. Charlot, and E. Djurado, *Journal of Power Sources*, **450**, 227724 (2020).
24. G. Martinez-Criado, J. Villanova, R. Tucoulou, D. Salomon, J.-P. Suuronen, S. Laboure, C. Guilloud, V. Valls, R. Barrett, E. Gagliardini, Y. Dabin, R. Baker, S. Bohic, C. Cohen, and J. Morse, *Journal of Synchrotron Radiation*, **23**, 344–352 (2016).
25. V. A. Solé, E. Papillon, M. Cotte, Ph. Walter, and J. Susini, *Spectrochimica Acta Part B: Atomic Spectroscopy*, **62**, 63–68 (2007).
26. W. De Nolf, F. Vanmeert, and K. Janssens, *J Appl Cryst*, **47**, 1107–1117 (2014).
27. K. Thompson, D. Lawrence, D. J. Larson, J. D. Olson, T. F. Kelly, and B. Gorman, *Ultramicroscopy*, **107**, 131–139 (2007).
28. G. Sassone, E. Da Rosa Silva, M. Prioux, M. Hubert, B. Morel, A. Léon, and J. Laurencin, *ECS Transactions*, **111**, under preparation (2023).
29. Q. Fang, C. E. Frey, N. H. Menzler, and L. Blum, *J. Electrochem. Soc.*, **165**, F38–F45 (2018).
30. Y. Wang, C. Wu, B. Zu, M. Han, Q. Du, M. Ni, and K. Jiao, *Journal of Power Sources*, **516**, 230660 (2021).
31. M. Hubert, J. Laurencin, P. Cloetens, B. Morel, D. Montinaro, and F. Lefebvre-Joud, *Journal of Power Sources*, **397**, 240–251 (2018).
32. L. Rorato, Y. Shang, S. Yang, M. Hubert, K. Couturier, L. Zhang, J. Vulliet, M. Chen, and J. Laurencin, *Journal of The Electrochemical Society*, Accepted (2023).
33. M. Morales, V. Miguel-Pérez, A. Tarancón, A. Slodczyk, M. Torrell, B. Ballesteros, J. P. Ouweltjes, J. M. Bassat, D. Montinaro, and A. Morata, *Journal of Power Sources*, **344**, 141–151 (2017).
34. P. Hjalmarsson, X. Sun, Y. L. Liu, and M. Chen, *Journal of Power Sources*, **223**, 349–357 (2013).
35. H. Xu, K. Cheng, M. Chen, L. Zhang, K. Brodersen, and Y. Du, *Journal of Power Sources*, **441**, 227152 (2019).
36. A. Tsoga, A. Naoumidis, and D. Stöver, *Solid State Ionics*, **135**, 403–409 (2000).
37. V. Wilde, H. Störmer, J. Szász, F. Wankmüller, E. Ivers-Tiffée, and D. Gerthsen, *ACS Appl. Energy Mater.*, **1**, 6790–6800 (2018).
38. J. Szász, F. Wankmüller, V. Wilde, H. Störmer, D. Gerthsen, N. H. Menzler, and E. Ivers-Tiffée, *J. Electrochem. Soc.*, **165**, F898 (2018).